

SOLID POLYMER ELECTROLYTES WITH SACRIFICIAL END GROUPS FOR A WIDE OXIDATIVE POTENTIAL AND STABLE INTERFACE IN LITHIUM METAL BATTERIES

Ashish Raj^a, Satyannarayana Panchireddy^a, Lieven Bekaert^{bc}, Bruno Grignard^{de}, Christophe Detrembleur^{de}, and Jean-François Gohy^a

^a*Institute of Condensed Matter and Nanoscience (IMCN), UCLouvain, Place L. Pasteur 1, 1348 Louvain-la-Neuve, Belgium*

^b*Electrochemical and Surface Engineering (SURF), Department of Materials and Chemistry, Vrije Universiteit Brussel, 1050 Brussels, Belgium*

^c*Eenheid Algemene Chemie (ALGC), Vrije Universiteit Brussel (VUB), 1050 Brussels, Belgium*

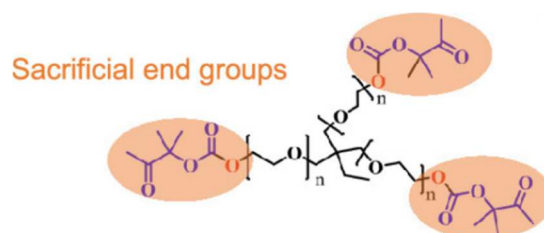
^d*Center for Education and Research on Macromolecules (CERM), CESAM Research Unit, University of Liège, 13 Allée du 6 août, Building B6A, 4000 Liège, Belgium*

^e*Federation of Researcher in Innovation Technologies for CO₂ Transformation (FRITCO2T Research Platform), University of Liège, 13 Allée du 6 août, Building B6A, 4000 Liège, Belgium*

Keywords: PEG, LiTFSI, electrolytes, interface, lithium batteries

Abstract

Poly(ethylene glycol) (PEG), despite being the most studied polymer electrolyte, suffers from serious drawbacks, which require fundamental studies behind its underperformance in lithium batteries. Here, we report the effect of the terminal group on triarm PEG stars bearing either hydroxyl (TPEG-OH) or carbonate-ketone (TPEG-Carb-ket) terminal groups. The latter is synthesized by a ring-opening reaction triggered by the -OH end group of TPEG-OH and results in a carbonate-ketone functionality. Indeed, the modified chain end is found to act as a sacrificial group by focusing the reactivity of the chain on the terminal group, protecting the rest of the TPEG molecule, which significantly reduces interfacial degradation and achieves a broader electrochemical stability window of up to 4.47 V, high Coulombic efficiency, and capacity retention. It furthermore demonstrates a stable interface with lithium metal after more than 1200 h of stripping and plating. When those electrolytes are investigated in reference cells based on LiFePO₄ cathodes and Li anodes, the change in discharge capacity is observed from 118.7 to 113.8 and 108.9 to 5.03 mAh g⁻¹ for TPEG-Carb-ket and TPEG-OH electrolytes, respectively, from the 1st to 100th cycle. The experimental results are further supported by density functional theory calculations and ab initio molecular dynamics simulations.



Introduction

Batteries have become a vital part of our daily life due to their small-scale to large-scale device applications with rechargeable lithium-ion batteries (LIBs) as a front-runner for two to three decades, catering the energy storage needs due to their higher energy density than conventional batteries.

Nevertheless, at present, the energy and power densities of LIBs are insufficient to meet the future demand for electric vehicles and hence require more innovation. This suggests the replacement of graphite- and silicon-based anodes with the lithium metal anode due to its higher theoretical capacity (3860 mAh g^{-1}) and lighter weight. (1,2) However, lithium metal batteries (LMBs) with liquid electrolytes pose several drawbacks, of which safety is of the greatest concern. Most of these conventional electrolytes are volatile solvents, flammable, and thermally unstable and do not offer facile recyclability and postutilization. Furthermore, their packaging holds a serious risk of electrolyte leakage, draining, and internal heating, leading to loss of assets and life. (3–5) In this context, replacing the liquid electrolyte-soaked separator with a mechanically stable solid membrane is believed to prevent lithium dendrite growth and contribute to higher energy density ($\sim 250 \text{ WhK g}^{-1}$). (6,7) This is why a pragmatic shift toward solid-state electrolytes (SSEs) has given hope for safe batteries as opposed to conventional liquid electrolyte-based batteries. Among SSEs, solid polymer electrolytes (SPEs) have emerged as interesting candidates. One of the first reports of SPEs has been credited to Armand for his discovery of poly(ethylene glycol) (PEG) as a lithium ion conductor. (8) Following this seminal work, various classes of polymers, graft- and copolymers, networks, blends, gels, and hybrid materials based on PEG have been investigated. (9–12) Moreover, designing an electrolyte with good ionic conductivity, wide electrochemical stability window (ESW), high transference number, and high dielectric constant, and an interface compatible with superior mechanical and thermal properties remains a key challenge at present. (3,13–15) Although the discovery of PEG as the polymer electrolyte (PE) was a breakthrough, this material suffers from trade-offs, such as semicrystallinity (at RT) along with low oxidative potential and high reactivity with lithium metal. (16) In the last two decades, cathode materials, such as $\text{LiNi}_x\text{Mn}_y\text{Co}_{1-x-y}\text{O}_2$ (NMC), have been commercialized, and this, in turn, demands more thermally and mechanically stable electrolytes with a wide ESW of greater than 4.3 V. (17)

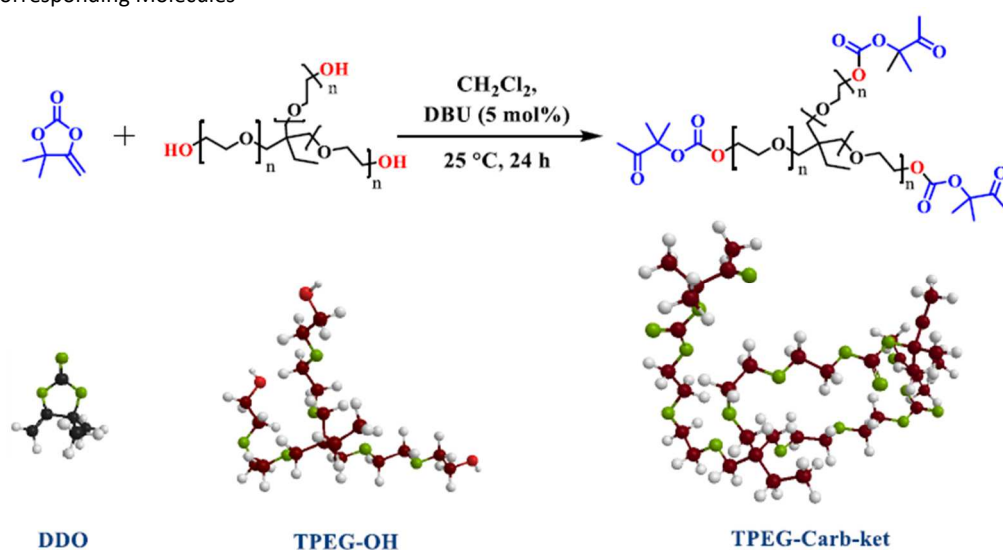
In addition to the ionic conductivity, interface design is also an important aspect of gel or solid-state batteries for limiting dendrite growth and parasitic reactions for a beneficial solid electrolyte interphase (SEI). Various methodologies have been adopted, such as catholytes incorporating PEs, the inclusion of film-forming additives, thin-layer polymer/inorganic surface coatings, etc. (18–24) Referring to some reports, Goodenough and co-workers (25) modified the anode–anode/cathode interface with poly(ethylene oxide)/poly(*N*-methyl-malonic amide) and observed an ESW greater than 4.25 V. Most importantly, it is essential to understand the reactions of the polymer at the interfaces and predict the beneficial decomposition of electrolytes for stable interfaces. Nowak and co-workers (26) highlighted various decomposition products of ethylene carbonates and unveiled the pathway of their decomposition. Sun and co-workers (27) and Wang and co-workers (28) showed how the terminal functional group within PEG derivatives affects the reactivity of the electrolyte and proves to be beneficial in engineering a stable interface with the lithium anode in addition to the ESW widening to 4.3 V for a higher energy density. While the ether units in PEG contribute to the transport of lithium ions due to the ion hopping between the oxygen atoms, (29) it is not very clearly understood which role the hydroxyl end group plays in terms of its reactivity with lithium metal. In those previous studies, it was demonstrated that replacing the hydroxyl end groups of PEG with ether/epoxy groups can hinder the side reactions with lithium metal in addition to stabilizing the interface. (27,28) Introducing

suitable chemical moieties at the chain end of PEG-based SPEs therefore seems to be a valuable strategy for the formation of stable SEIs in LMBs.

The fact that carbonate functional groups are widely used in current liquid electrolytes motivated researchers to introduce carbonate groups in SPEs. As typical examples, Tominaga and co-workers (30) combined carbonate and ether units in a copolymer, which was obtained by copolymerization of ethylene oxide with CO₂. One of our previous works involved electrolytes based on cyclic carbonate trifluoromethacrylate bearing vinylidene fluoride units (31) and random copolymers of *n*-butyl acrylate and cyclic-carbonate-bearing acrylate. (32) Carbonates are well-known to react with metal lithium to form a complex SEI, but, in the case of carbonate-based SPEs, this reaction is limited at the interface with the lithium anode and allows the formation of a stable SEI and of an extended ESW compared to poly(ether)-based SPEs. (31–34) However, the ionic conductivity in those carbonate-based SPEs is lower than in poly(ether) systems, limiting their use in LMBs. (31–34)

Here, we propose to combine the best of both worlds by modifying the chain ends of poly(ether)-based SPEs by carbonate groups. As a polymer, we have selected a commercially available low molar mass triarm PEG (TPEG-OH) because this polymer contains three terminal reactive hydroxyl groups, is a viscous liquid under ambient conditions, and is prone to show a high ionic conductivity at RT when loaded with lithium salt. In the second step, we will modify the hydroxyl end groups of TPEG-OH via a facile ring-opening reaction with a cyclic carbonate at RT (refer to Experimental Section and Scheme 1). This will allow the formation of carbonate-ketone end-functionalized TPEG (TPEG-Carb-ket), whose behavior will be systematically compared to that of TPEG-OH-based SPEs. A comparative detailed study on the electrochemical properties of both polymers will be performed, including conductivity, voltammetry, and battery prototypes with LiFePO₄ cathodes. The experiments will be supported by density functional theory (DFT) calculations to compare the reactivity of Carb-ket to –OH. Ab initio molecular dynamics (AIMD) simulations of the electrode–electrolyte interfaces will also be realized. In the quest of achieving longer lifetime and higher energy density batteries, those kinds of studies can be groundbreaking, with interfacial chemistry guiding the design of sustainable and additive-free all-solid-state LMBs.

Scheme 1. Synthesis of Triarm Poly(ethylene glycol) Carbonate Ketone (TPEG-Carb-ket) with 3D Structures of the Corresponding Molecules



Experimental Section

Materials and Methods. Poly(ethylene glycol) trimethylolpropane ether (TPEG-OH) ($M_w \sim 450$ g/mol), 1,8-diazabicyclo (5.4.0) undec-7-ene (DBU) (98%), lithium bis(trifluoromethanesulfonyl)imide (LiTFSI), lithium iron phosphate (LiFePO₄/LFP), poly(vinylidene fluoride) (PVDF), and Super P were purchased from Sigma-Aldrich. *N*-methyl-2-pyrrolidone (NMP) was purchased from Alfa Aesar. 4,4-Dimethyl-1,3-dioxolan-2-one (DDO) was synthesized by carboxylative coupling of CO₂ with 2-methyl-3-butyne-2-ol using a CuI/tetrabutylammonium phenolate dual catalyst, following a previously reported protocol. (35) Deuterated chloroform (CDCl₃) used for NMR spectroscopy was purchased from Eurisotop. Cellulose fiber paper was purchased from TOB. All reactants and catalysts were used as received, without any further purification.

Characterization Techniques. *Nuclear Magnetic Resonance.* Nuclear magnetic resonance (NMR) spectroscopy was conducted using a Bruker 300 UltraShield spectrometer. The monomers and polymers were dissolved in CDCl₃.

Fourier-Transform Infrared Spectra Measurements. Fourier-transform infrared (FTIR) spectra measurements were carried out on a PerkinElmer spectrometer, equipped with a diamond attenuated transmission reflectance device. Eight scans were recorded for each sample over the range of 4000–500 cm⁻¹ with a normal resolution of 4 cm⁻¹ and spectra were analyzed with Spectra quanta software.

Differential Scanning Calorimetry. Differential scanning calorimetry (DSC) was conducted using a Mettler Toledo DSC1 instrument, equipped with STARe software. Samples were placed in a 40 μL sealed aluminum pan. The temperature profile was swept from –70 to 100 °C at a heating rate of 10 °C min⁻¹ under a nitrogen atmosphere.

Thermogravimetric Analysis. Thermogravimetric analysis (TGA) was conducted using a Mettler Toledo thermogravimetric analyzer. Samples were placed in an 85 μL alumina crucible under a constant argon flow with a heating rate of 5 K min⁻¹, and the initial and final temperatures were set at 25 and 600 °C, respectively.

X-ray Photoelectron Spectroscopy. X-ray photoelectron spectroscopy (XPS) was performed using an SSI X-Probe (SSX 100/206) photoelectron spectrometer from Surface Science Instruments, equipped with a monochromated Al Kα (200 W) X-ray source. The batteries were disassembled, and samples were mounted on an XPS sample holder in a glovebox prior to transferring to the XPS vacuum chamber in the flux of an argon atmosphere. All binding energies were calculated relative to the C– (C, H) component of the C 1s peak fixed at 284.8 eV. Data analysis was carried out by using CasaXPS software. For the survey scan, a 1.0 eV step size was used, and a 0.1 eV step size was used for high-resolution scans for all elements with 150 energy steps.

Electrochemical Analysis. Electrochemical analysis of potentiostatic electrochemical impedance spectroscopy (PEIS), linear sweep voltammetry (LSV), chronoamperometry (CA), and galvanostatic cycling potential limitation was carried out on Biologic BCS-COM and VMP3 multichannel potentiostats using CR2032 coin cells.

Potentiostatic Electrochemical Impedance Spectroscopy. The ionic conductivity of TPEG analogue PEs was determined by PEIS using symmetric stainless steel (SS) (SS | PE_{x%} | SS) with a Teflon (PTFE) ring in

Swagelok cells over the frequency range of 7 MHz–50 mHz, with an applied single sinusoidal A.C. excitation voltage of 10 mV. The temperature dependence measurements were carried out from 20 to 100 °C by gradually increasing the temperature at a rate of 0.33 °C min⁻¹. One hour was allowed to pass between each measurement to reach an equilibrium state.

Linear Sweep Voltammetry. Measurements were performed at various temperatures on asymmetric CR2032 coin cells as (Li|PE_{x%}|Al) and (Li|PE_{x%}|SS) over the potential range of 0–6 V (vs Li/Li⁺) at a scan rate of 1 mV s⁻¹ at 30 °C.

Transference Number. Transference number (t_{Li^+}) measurements were carried out on symmetric lithium metal cells (Li|PE_{x%}|Li) fabricated over various membranes by following the Bruce–Vincent method. CA with a DC voltage of 10 mV was performed, followed by PEIS measurements in the frequency range of 7 MHz–50 mHz, using an AC excitation voltage of 10 mV at 30 °C. PEIS measurements were recorded before and after the steady state (before and after polarization).

Stripping and Plating. The symmetric cell Li|PE_{x%}|Li was fabricated for stripping and plating analysis. The cells were charged and discharged for 1 h each for multiple cycles with a current density of 1 μA cm⁻² and cutoff voltages of +4 V and -4 V at room temperature using a BioLogic BCS-COM multichannel potentiostat.

Galvanostatic Cycling Potential Limitation. Galvanostatic charge–discharge cycling and rate capability measurements for the Li|PE_{x%}|LFP cells were tested with a Biologic BCS-COM cyler. The slurry for the cathodes was prepared from LiFePO₄, Super P, PVDF, and NMP via grinding using a mortar pestle and cast on Al-foil/carbon with a doctor-blade technique. The coated slurry was dried in an air oven for more than 6 h at 60 °C prior to vacuum drying at 120 °C for more than 24 h. The cathode compositions were maintained to a weight ratio of 7:2:1 for LFP (70 wt %), Super P (20 wt %), and PVDF (10 wt %) slurry, respectively. The cathode and anode were cut into a diameter of 14 mm for electrolyte films with a diameter of 16 mm for the cell assembly.

Synthesis. *Synthesis of Three-Arm Poly(ethylene glycol) Carbonate Ketone.* TPEG-Carb-ket was synthesized by the reaction of DDO (3.05 eq., 2.60 g, 0.02 mol) with TPEG-OH (M_w = 450 g/mol, 1 eq., 3 g, 0.0066 mol) using 10 mL of dry CH₂Cl₂. The reaction, catalyzed by DBU (5 mol % vs TPEG-OH, v = 50 μL), was performed for 24 h at 25 °C. After the reaction, the TPEG-Carb-ket product was collected by simple removal of the solvent and DDO residues by high vacuum for 24 h. These optimized reaction conditions ensured the fast and complete ring opening of the DDO-disubstituted cyclic carbonate by the hydroxyl groups of TPEG. The reaction resulted in the change of color from transparent to light brownish with an increase in viscosity.

Preparation of Electrolytes (SEs). All the electrolytes were prepared by mixing TPEG analogues with a given amount of LiTFSI (0–50 wt %). The obtained viscous solutions were coated on a cellulose separator for coin cell fabrication. The separator support was used in the preparation of electrolytes to provide the self-standing ability to the films without the need for cross-linking and to control the thickness of the PEs. Coin 2032-type cells were assembled using free-standing PE films (50–150 μm) sandwiched between SS|Li, Li|Al, Li|Li, and Li|LFP electrodes to evaluate their electrochemical performance.

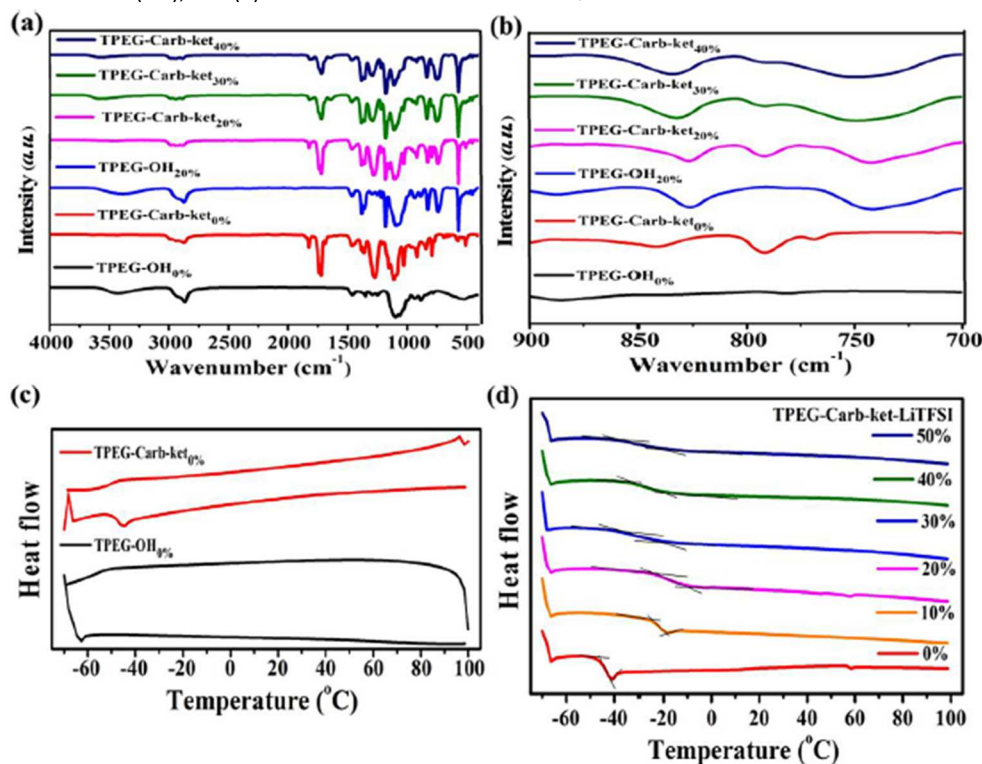
Theoretical Calculations. Quantum chemical calculations were performed with the Gaussian 16 Revision A.03 program (36) using the DFT B3LYP functional, Grimme's dispersion (D3BJ), and ultrafine integration. (37,38) Structure optimization was performed for the molecular structures shown in Figure S9 with the 6-31+G(d) basis set, and a frequency calculation was performed to verify the absence of imaginary frequencies. Single-point energy calculations were performed with the 6-311+G(d,p) basis set. From the obtained structures, HOMO and LUMO energy levels were obtained. AIMD simulations were performed using the Vienna Ab initio Simulation Package (VASP) (vasp.5.4.4) (39) using the projector augmented wave (PAW) method (40) and the Perdew–Burke–Ernzerhof generalized gradient approximation as the exchange–correlation functional. (41) The plane-wave cutoff was set to 550 eV, and a Gaussian smearing with a width of 0.1 eV was used. A $2 \times 2 \times 1$ Monkhorst and Pack k-point mesh was used to sample the Brillouin zone and the zero damping DFT-D3 method of Grimme was used to account for van der Waals corrections. (42) All simulations were run for 5000 fs using the Verlet integration algorithm. The temperature was set to 400 K and the velocities were rescaled every 4 steps. The electronic self-consistency convergence condition was set to 10^{-5} eV. The VESTA software package was used to visualize molecular structures. (43) Bader charge analysis was performed using the Bader package. (44)

Results and Discussion

Synthesis of Solid Polymer Electrolytes. The organocatalyzed ring opening of DDO by primary alcohol is facile at room temperature, delivering a ketone-carbonate (Carb-ket) group. (45,46) It was exploited for converting the hydroxyl groups of TPEG-OH (in the presence of DBU as the catalyst) into carbene-ket, as shown in Scheme 1. The transformation of the TPEG into TPEG-Carb-ket was evidenced by ^1H NMR spectroscopy. Figure S1 reveals the appearance of the characteristic methyl protons of the acetyl chain ends at 2.16 ppm and of the methylene adjacent to the carbonate linkage at 4.26 ppm. The yield of functionalization, estimated to be 97%, was determined from the ^1H NMR spectrum by comparison of the relative intensities of the methyl signals of the acetyl chain ends with the methyl group of the TPEG initiator at 0.83 ppm. We also noted the presence of residual DDO with peaks on very low intensities at 4.75 and 4.30 ppm assigned to the exocyclic vinylene moiety and at 1.64 ppm relative to the methyl groups. The other proton signals in TPEG-Carb-ket were identical to the TPEG-OH skeleton. TPEG-OH and TPEG-Carb-ket were then mixed with various amounts of LiTFSI in order to obtain SPE membranes (see Experimental Section for details). In the following formulations, the wt% of added LiTFSI is indicated as a subscript for either TPEG-OH or TPEG-Carb-ket samples. The electrolyte samples were then analyzed by FTIR spectroscopy. For TPEG-Carb-ket, the ring opening of DDO was confirmed by FTIR (Figure 1a) with the presence of bands corresponding to the $\text{C}=\text{O}$ stretching at 1740 cm^{-1} originating from the linear cyclic carbonate and at 1722 cm^{-1} from the ketone group and the absence of $\text{O}-\text{H}$ stretching at 3430 cm^{-1} . The sharp yet less intense band at 1826 cm^{-1} can be attributed to unreacted cyclic carbonate from excess DDO supported by the weak band at 1687 cm^{-1} that could be attributed to $\text{C}=\text{C}$ stretching of DDO. (33) The broadening in the asymmetric $\text{C}-\text{O}$ stretching band from carbonyl associated with TPEG-Carb-ket can be observed in the range of $1270\text{--}1295\text{ cm}^{-1}$. Other characteristic peaks corresponding to LiTFSI were recorded at 1181 cm^{-1} for SO_2 asymmetric stretching

and at 739–750 cm^{-1} for S–N–S symmetric stretching. The solvation of LiTFSI could be confirmed by the $\text{O}_n\text{-Li}^+$ breathing mode around 827 cm^{-1} for all of the TPEG analogues as generally observed for short PEG chain-based SPEs (Figure 1b). (47–50)

Figure 1. (a) IR spectra of TPEG-OH and TPEG-Carb-ket, respectively, with and without LiTFSI (subset indicates the wt% of salt in the polymer); (b) ATIR in the region of 900–700 cm^{-1} as of panel (a); (c) DSC thermograms of TPEG-OH and TPEG-Carb-ket without LiTFSI (0%); and (d) DSC exocurve of TPEG-Carb-ket_{x%} with variable LiTFSI concentrations.



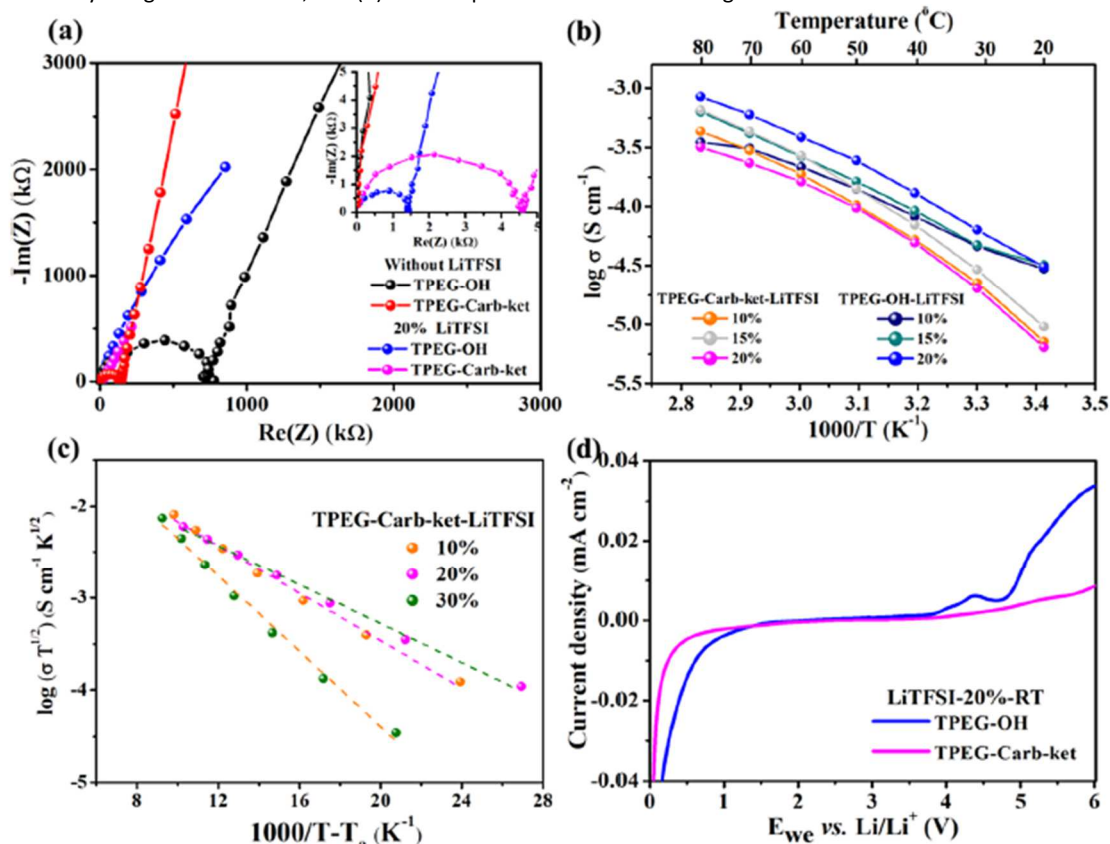
Thermal Properties of Solid Polymer Electrolytes. DSC was performed on TPEG analogues to investigate the effect of the modified chain ends on the glass-transition temperature (T_g). In the exothermic and endothermic curves for TPEG-OH and TPEG-Carb-ket (Figure 1c), the T_g was observed at -43.6°C for TPEG-Carb-ket and -61.1°C for TPEG-OH. Both polymers did not show crystallinity which was neither expected given their low molecular weight and viscous liquid-like nature. The effect of salt concentration on T_g was analyzed for 0–50 wt % LiTFSI dissolved in TPEG-Carb-ket (Figure 1d). The DSC curves indicate that the T_g increased from -43.6 to -17.15°C for 0–20% LiTFSI due to the ion–polymer interactions. (51) At higher concentrations, not all the lithium salts coordinate with oxygen, and the excess salt leads to the formation of aggregates acting as plasticizers and resulting in a lower T_g (Table 1). (34) The TGA of TPEG-Carb-ket and TPEG-OH with and without LiTFSI has been performed and is depicted in Figure S2.

Table 1. Activation Energy and Pre-exponential Factor as Calculated from the Slope of VFT Plots with TGA (T_s) Temperature Stability

TPEG-Carb-ket-LiTFSI	$T_s (^{\circ}\text{C})$	$T_g (^{\circ}\text{C})$	R^2	$E_a (\text{kJ mol}^{-1})$
0%	115.11	-43.57		
10%		-21.80	0.999	2.0
20%	108.76	-17.15	0.996	3.9
30%		-28.20	0.993	2.5

Conductivity. PEIS was performed in order to determine the ionic conductivity of the LiTFSI-loaded TPEG-OH and TPEG-Carb-ket samples (see Experimental Section). The resulting Nyquist plots have been analyzed to measure the conductivity at different temperatures. The Nyquist plots (Figure 2a) show PEIS of TPEG-OH and TPEG-Carb-ket with and without LiTFSI (refer to Figure S3a,b for other PEIS studies). For pure polymer samples without LiTFSI, a conductivity of $2.6 \times 10^{-7} \text{ S cm}^{-1}$ was measured for TPEG-Carb-ket, while a value of $6.7 \times 10^{-8} \text{ S cm}^{-1}$ was observed for TPEG-OH. Although this method makes it difficult to completely discriminate between the ionic and electronic conductivity of the polymer, we assume that the measured conductivities without LiTFSI can be attributed to the electronic conductivity. The conductivity of the electrolytes formed by TPEG-OH and TPEG-Carb-ket added with various amounts of LiTFSI (10–20 wt %) was then investigated as a function of temperature, as depicted in Figures 2b and S3c, using the Arrhenius conductivity model. As expected, conductivity values increased with temperature as a result of the increased chain segment motion. The conductivity of TPEG-Carb-ket loaded with LiTFSI was always slightly lower than that of TPEG-OH-LiTFSI electrolytes, and the difference was more noticeable at room temperature (Figure 2b). To sum up, it was found that despite an identical number of ether groups in the TPEG-OH and TPEG-Carb-ket samples, the ionic conductivity was decreased in TPEG-Carb-ket, emphasizing the detrimental effect of carbonate-ketone groups at the chain end on the T_g of the electrolyte and hence on its conductivity.

Figure 2. (a) Nyquist plot of TPEG analogues as a result of PEIS at 30 °C with and without LiTFSI; (b) temperature-dependent ionic conductivity for triarm TPEG analogue PE with reinforced LiTFSI (10–20 wt %); (c) temperature-dependent ionic conductivity using the VFT model; and (d) LSV comparison of the TPEG analogues with 20% LiTFSI at RT.



In order to elucidate the influence of the polymer segments in the context of the Vogel–Fulcher–Tammann (VFT) behavior, the VFT Equation 1 was used to fit the conductivity data with respect to the glass transition of TPEG-Carb-ket in the 20–80 °C temperature range:

$$\sigma T^{1/2} = A e^{-E_a/kb(T-T_0)} \quad (1)$$

where A is the pre-exponential factor, T is the absolute temperature, T_0 is the Vogel scaling temperature at which the free volume disappears or at which free entropy becomes zero, T_0 is approximated as $T_g - 50$ K, E_a is the pseudoactivation energy of ion transport, and k_b is the Boltzmann constant. (52–54) Given the low chain length and viscous nature of the polymer, chain-segment motion cannot be neglected. The linear fitted VFT conductivity plot clearly supports the phenomena above T_g of the polymer (Figure 2c). Therefore, we inferred that the ionic conductivity was obtained as a result of Li-ion hopping coupled to segmental motion in the TPEG-Carb-ket group. The activation energy as calculated from the VFT plot was calculated along with the pre-exponential factor and R^2 as the corresponding fitting coefficient and has been depicted in Table 1.

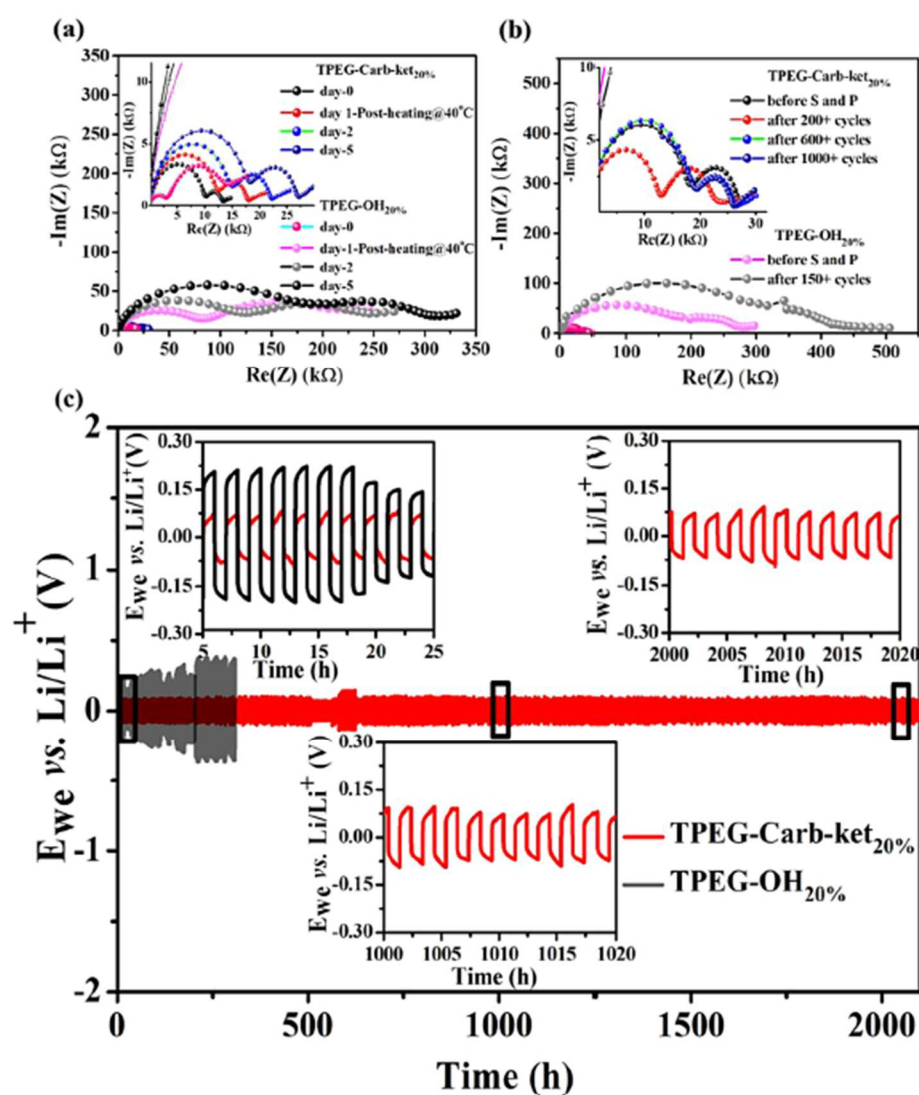
Linear Sweep Voltammetry. LSV was performed for TPEG-OH and TPEG-Carb-ket to investigate the redox behavior in cathodic and anodic regions (Figure 2d). The oxidation limit of TPEG-Carb-ket was noted to be ~4.5 V in contrast to ~3.9 V for TPEG-OH. We did not observe any Al corrosion or electrolyte degradation for TPEG-Carb-ket. A higher cutoff current density and an oxidation peak clearly indicated the faradaic reaction in the case of TPEG-OH, in agreement with the behavior usually observed for PEG-based electrolytes. It thus seems that the terminal ketone-carbonated end groups in the TPEG-Carb-ket sample have a beneficial effect on the electrochemical stability. The LSV measurements with variable LiTFSI concentrations with Li|SS electrodes were also performed and analyzed, as mentioned in the Supporting Information (Figure S3d). Electrolytes with a higher oxidation potential such as TPEG-Carb-ket make them interesting candidates for high-voltage cathode batteries. (55,56)

Aging Study and Stripping–Plating. A dendrite-free stable interface with lithium metal is a key challenge for the practical application of LMBs. Prior to stripping and plating, we performed the aging study by PEIS for the Li–Li cells at the open-circuit potential (OCP). (57,58) In Figure 3a,b, the Nyquist plots for TPEG-OH_{20%} and TPEG-Carb-ket_{20%} show the evolution of the resistance from day 0 to day 5. The bulk electrolyte resistances for TPEG-OH_{20%} and TPEG-Carb-ket_{20%} were 3.03 and 10.22 kΩ on day 0, respectively. Then, both cells were heated at 40 °C for stabilization of the interface prior to impedance measurements. A drastic increase in the bulk resistance can be observed for TPEG-OH_{20%} over time, while a much less steep increase was observed for TPEG-Carb-ket, as observed in Table 2. The decomposed electrolyte species at the OCP are responsible for this increase in bulk resistance, resulting in the formation of an SEI at the lithium surface. Figure S4b shows that R_{elec} increases drastically at the OCP for TPEG-OH_{20%} even without heating. Similar results are obtained for cells with copper and lithium as the anode and cathode, respectively, as shown in Figure S4a. Those results clearly indicate that the TPEG-OH_{20%} sample is much more prone to decomposition than the TPEG-Carb-ket sample when it is brought in contact with lithium.

Table 2. Electrolytic (R_b) and Interfacial Resistance (R_{in}) as a Result of Aging in Li Symmetric Cells (R is Given in kOhm/kΩ)

day	at OCP			
	TPEG-OH		TPEG-Carb-ket	
	R_b	R_{in}	R_b	R_{in}
0th	3.03	14.30	10.22	13.38
1st	83.73	233.36	12.61	18.14
2nd	124.59	246.01	15.10	22.37
5th	203.88	314.83	18.51	27.30

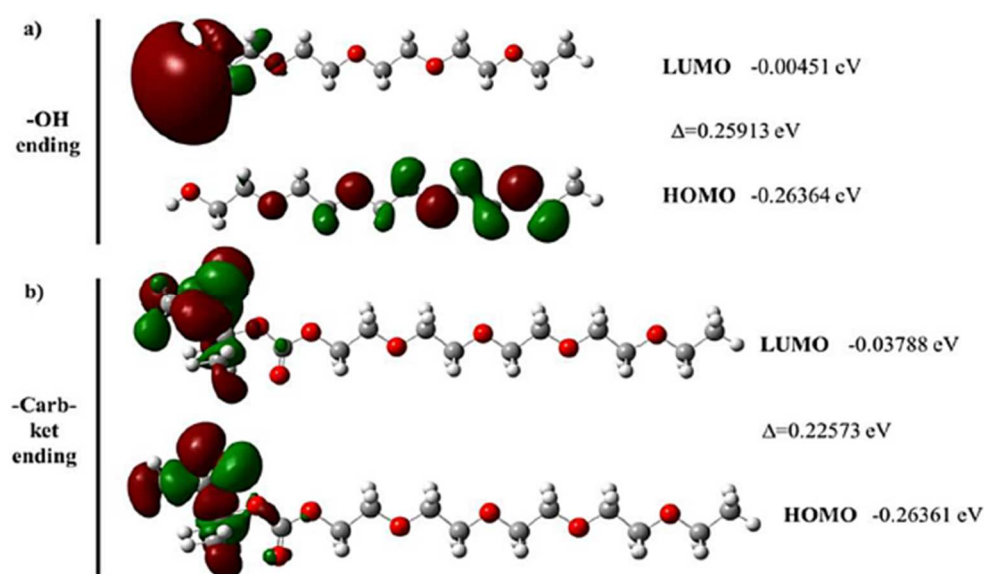
Figure 3. (a) Aging studies: PEIS with time at the open-circuit potential (OCP); (b) PEIS before and after stripping–plating; (c) galvanostatic charge–discharge voltage profile for stripping–plating at RT of both the Li|TPEG-OH_{20%}|Li cell and the Li|TPEG-Carb-ket_{20%}|Li cell (magnified plot in the inset).



In order to get further insight into those results, DFT calculations were performed on single-chain TPEG-OH and TPEG-Carb-ket terminal regions (structures shown in Figure S9). For the TPEG-Carb-ket sample, the HOMO and LUMO orbitals were found to be localized on the Carb-ket ending.

This contrasts with TPEG-OH, where in particular, the HOMO is spread out over the entire chain. This indicates that, in TPEG-Carb-ket, the reactivity is concentrated in the terminal group, which acts as a protection to the further inward chain, as opposed to TPEG-OH. Furthermore, even though the HOMO energies are similar, the LUMO energy is more negative (-0.03337 eV) for TPEG-Carb-ket, indicating that TPEG-Carb-ket can be reduced more easily, as shown in Figure 4. Those findings on the orbital locations and energies, combined with the experimental findings, suggest that the Carb-ket terminal group acts as a sacrificial group by focusing the reactivity of the chain on the terminal group and further protecting the bulk chain. This higher reactivity obviously results in a more stable SEI layer formation and is confirmed by the lower impedance observed experimentally.

Figure 4. HOMO and LUMO orbital structures with accompanying energies and HOMO–LUMO energy differences: (a) –OH terminal group molecule and (b) –Carb–ket terminal group molecule.



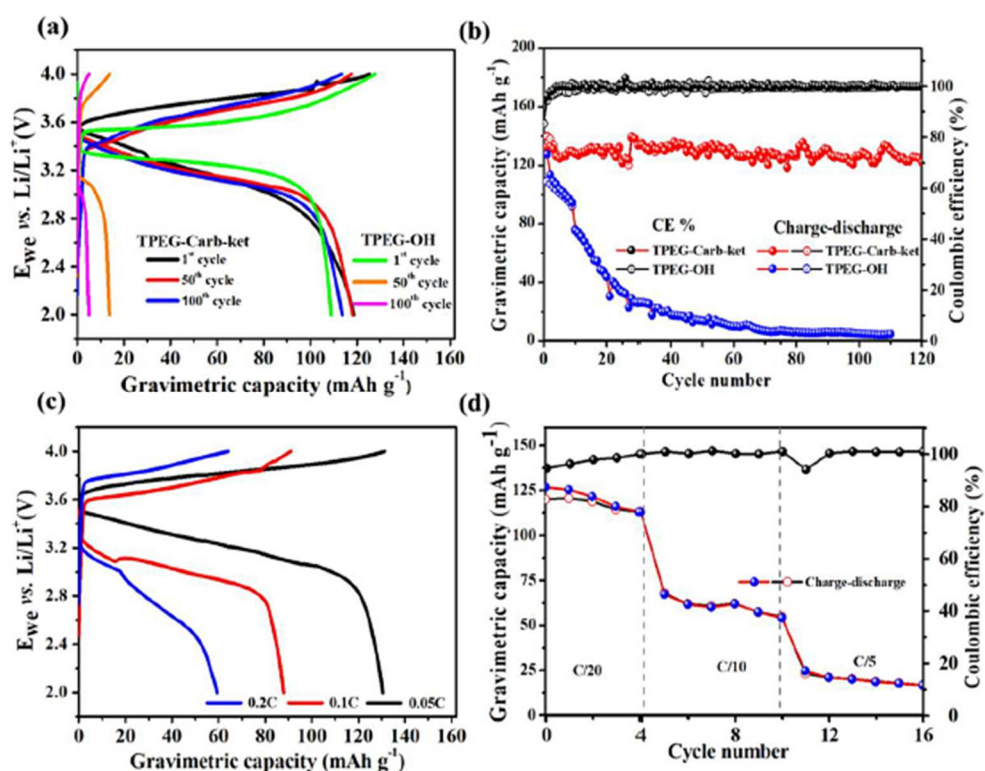
Time-dependent galvanostatic charge–discharge was then performed to shed light on the reversible stripping/plating of lithium in symmetric Li–Li cells. The experiments were performed for both TPEG-OH_{20%} and TPEG-Carb-ket_{20%} samples for ≥ 250 and ≥ 2000 h, as demonstrated in Figure 3c. The lower current density of $1 \mu\text{A cm}^{-2}$ was selected in order to allow overpotential monitoring in both polymers at RT. Both cells were heated to 40°C in order to equilibrate the interfaces prior to charge–discharge measurements. As it can be seen in Figure 3c for TPEG-OH_{20%}, the net overpotential gradually builds up in subsequent cycles from ≥ 190 to ≥ 350 mV in the span of ~ 150 cycles. This could indicate that the SEI is not stabilized at the interface despite lower current density. Even after conditioning the cell at rest for >46 h after ~ 100 cycles, slow decomposition of electrolytes still occurred, resulting in an unstable SEI for TPEG-OH_{20%}. While in the case of TPEG-Carb-ket_{20%}, the stripping–plating is observed to be far more efficient than that in the case of TPEG-OH_{20%}.

Despite the slight lower ionic conductivity than TPEG-OH_{20%}, TPEG-Carb-ket_{20%} recorded a lower overpotential of ≥ 70 mV during initial cycles and was observed to remain constant or slightly decreased after 1000 cycles, as shown in Figure 3c. After conditioning the cells at rest for 24 and 56 h after ~ 150 cycles and 400 cycles, respectively, no significant change in overpotential was observed in sharp contrast to TPEG-OH_{20%}. Finally, we investigated the conductivity as a result of SEI formation and

decomposition of electrolytes by PEIS after those long charge–discharge cycles. Clearly, the interfacial resistance is 10 times higher for TPEG-OH_{20%} than for TPEG-Carb-ket_{20%}. Obviously, the modified chain end in TPEG-Carb-ket_{20%} leads to the formation of a stable SEI and the superior transport of Li⁺ ions.

Lithium Metal Battery Prototypes. LMBs were fabricated by using lithium metal anodes and lithium ferrophosphate (LiFePO₄/LFP) cathodes for galvanostatic charge–discharge measurements. Room temperature cycling for TPEG-OH_{20%} and TPEG-Carb-ket_{20%} supported on a cellulose separator was performed in ambient conditions. In the voltage profile (Figure 5a) of Li|TPEG-OH_{20%}|LFP at a rate of 0.05C and RT, the polarization increased drastically from the 1st cycle to the 100th cycle while no significant change was noted in the case of Li|TPEG-Carb-ket_{20%}|LFP except a slight shift in oxidation voltage. For the TPEG-Carb-ket_{20%}-based cell, the discharge capacity of 118.7, 118.3, and 113.8 mAh g^{−1} was achieved for the 1st, 50th, and 100th cycle, respectively, whereas, for the TPEG-OH_{20%}-based cell, the discharge capacity of 108.9 mAh g^{−1} from the first cycle was drastically reduced to 13.8 and 5.03 mAh g^{−1} for the 50th and 100th cycle, respectively.

Figure 5. (a) Galvanostatic charge–discharge voltage profile for the 1st, 50th, and 100th cycle at 0.05C and RT; (b) capacity retention plot with cycle number 0.05C at RT for Li|TPEG-carb-ket_{20%}|LFP and Li|TPEG-OH_{20%}|LFP, respectively; (c) galvanostatic charge–discharge voltage profile at different C-rates; and (d) rate capability plot with different C-rates for Li|TPEG-carb-ket_{20%}|LFP.

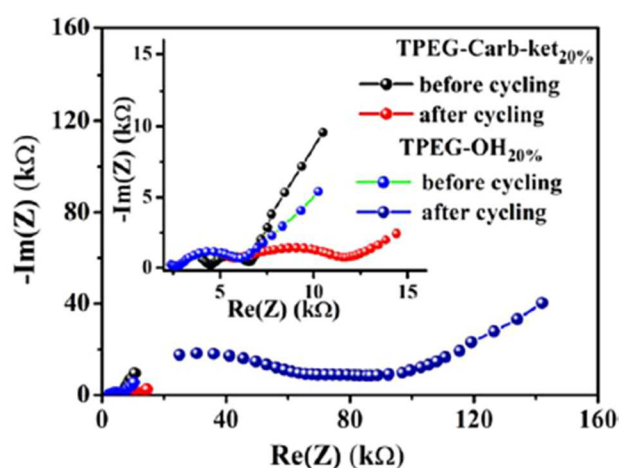


The parasitic reaction of TPEG-OH_{20%} with lithium metal is speculated to form unstable decomposed species offering higher resistance and polarization contrary to stable SEI in TPEG-Carb-ket. With the sacrificial effect of the terminal group in TPEG-Carb-ket as derived from the computational results, the lithium-ion conductivity is higher due to the more efficient and stable SEI layer formation.

The capacity retention for the Li|TPEG-Carb-ket_{20%}|LFP cell was calculated to be 95.8% while it only reached 4.6% for the Li|TPEG-OH_{20%}|LFP cell (Figure 5b) after 100 cycles. Further, the Li|TPEG-Carb-

ket_{20%}|LFP delivered the capacity of 130.4, 87.9, and 59.4 mAh g⁻¹ at 0.05C, 0.1C, and 0.2C rates, respectively. Higher polarization resulted in lower capacity at higher current density (Figure 5c,d). The poor performance of the TPEG-OH-based cells was also supported by the impedance measurements shown in Figure 6, with a clear indication of high bulk resistance in the former compared to the TPEG-Carb-ket-based cells. A comparison of cell performance for TPEG-OH and TPEG-carb-ket at 0.1C is detailed in the Supporting Information (Figure S6a). Again, those results confirm the superior performance of TPEG-Carb-ket-based cells. Furthermore, the specific capacity was further improved by increasing the concentration of charge carriers in the electrolyte with lower polarization. The voltage profile shown in Figure S7 for Li|TPEG-OH_{50%}|LFP and Li|TPEG-Carb-ket_{50%}|LFP cells shows higher capacity achieved at 0.1C. The capacity retention was also improved to 98.8% due to the improved conduction and transport properties.

Figure 6. Nyquist plot before and after cycling of Li|TPEG-OH_{20%}|LFP and Li|TPEG-Carb-ket_{20%}|LFP (magnified scale in the inset).



Postcycling XPS Analysis of Electrode Interfaces. The XPS analysis of the Li anode and TPEG-Carb-ket_{20%} electrolyte surface for Li–Li cells was performed to probe their interfacial composition after stripping and plating for ≥2000 h. The C 1s peak at 284.8 eV was used as a reference to calibrate the binding energy. (59) The major C and O elements could not be ignored from the XPS chamber or atmosphere and hence can also correspond to adventitious carbon. The survey spectra detected the expected elements like C, O, Li, F, N, and S originating from the SEI layer, as shown in Figure 7a, with abundance ratio % of elements in Figure 7b. The C 1s spectra in all samples (excluding the adventitious carbon) can be attributed to C–C/C–H, C–O/N, and C=O with the binding energies of ~284.8, 286.3, and 287.8 eV, respectively. Other O–(C=O)–O–(C=O)–O functional species have been detected at 289.1 and 289.8 eV, respectively, with speculated overlapping from inorganic carbonate (CO₃²⁻) as well, in the case of the Li metal surface and TPEG-Carb-ket on cellulose membrane (with a shift of 0.7 eV) (as shown in Figure 8a,d). (60) The bar chart corresponding to these species is plotted in Figure 7c, evidencing a higher amount of decomposed carbon species on the TPEG-Carb-ket surface than on the Li metal surface.

Figure 7. (a) Survey spectrum of the Li anode and TPEG-Carb-ket after cycling for more than 2000 h; (b) abundance ratio percentage of elements; and (c) bar chart showing the carbon functional species on Li and electrolyte surface constituting the SEI.

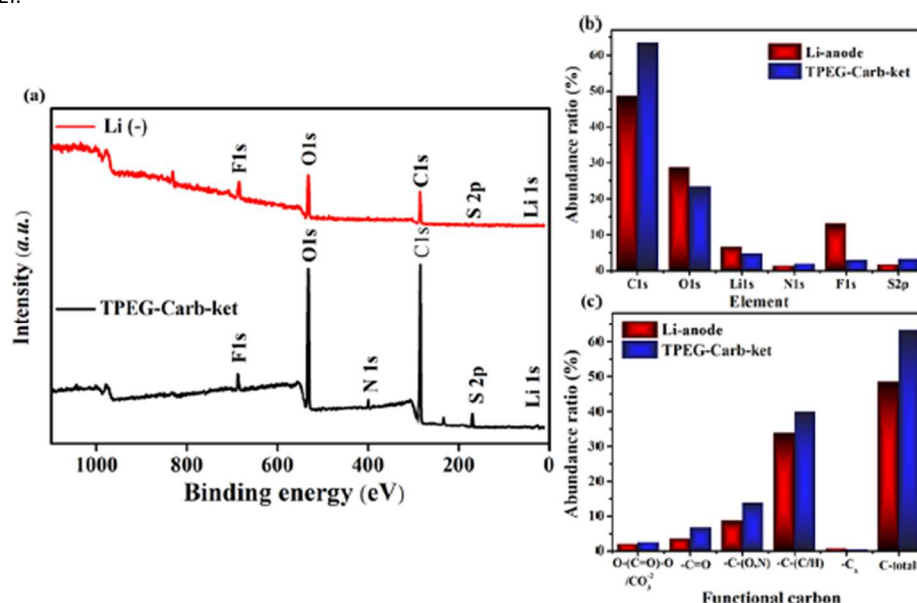
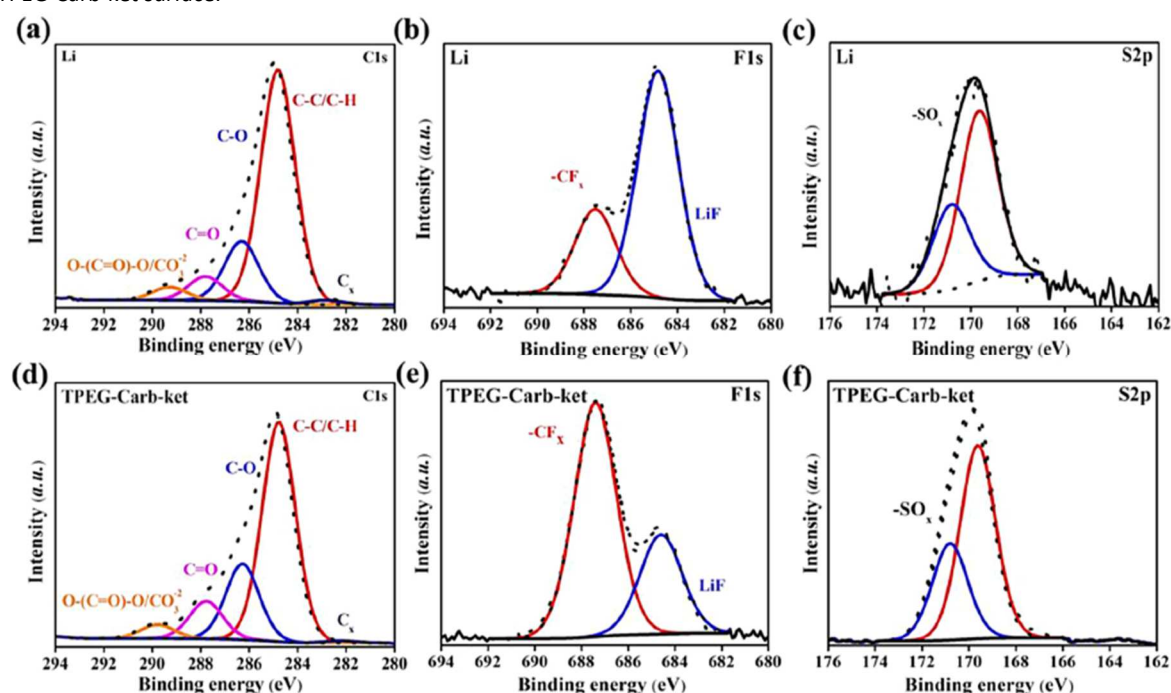


Figure 8. HR-XPS of (a,d) carbon (C 1s), (b,e) fluorine (F 1s), and (c,f) sulfur (S 2p) for decomposition at the lithium anode and TPEG-Carb-ket surface.

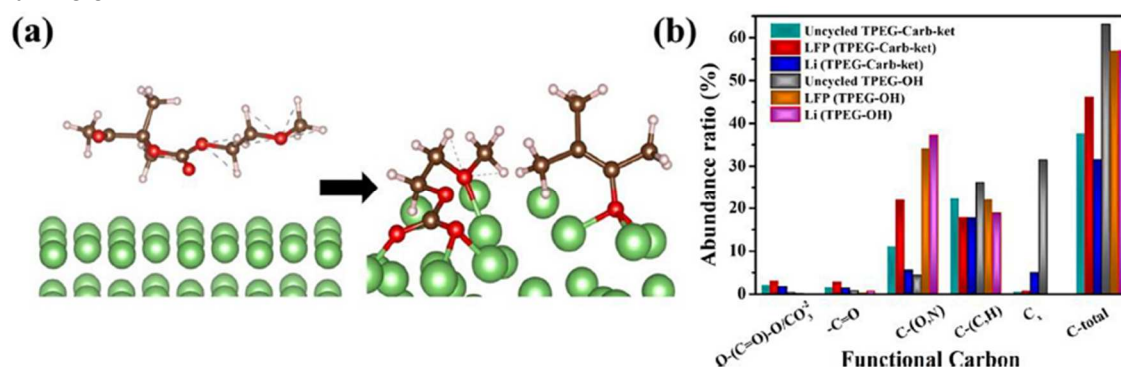


As a result of hundreds of cycles, interfaces were expected to contain a significant LiF amount, which was well witnessed from F 1s spectra in Figure 8b,e. In the case of the Li metal surface, the fluorine signals are constituted of 9.4% LiF and 3.7% -CF_x, while both fluorine species were also detected on TPEG-Carb-ket membranes with 2.2% -CF_x significantly higher than 0.8% LiF. The formation of LiF is a key parameter for a stable SEI and limited dendrite growth. (61–63) As far as the S 2p signals are concerned, the S 2p spectra in Figure 8c,f show the expected characteristic peaks of sulfone (-SO₂)

from LiTFSI at 169.6 and 170.7 eV. Additional XPS data (O 1s, Li 1s, and N 1s spectra, Figure S8 and Table S1) are discussed in the Supporting Information section, and the results are in line with the above discussion.

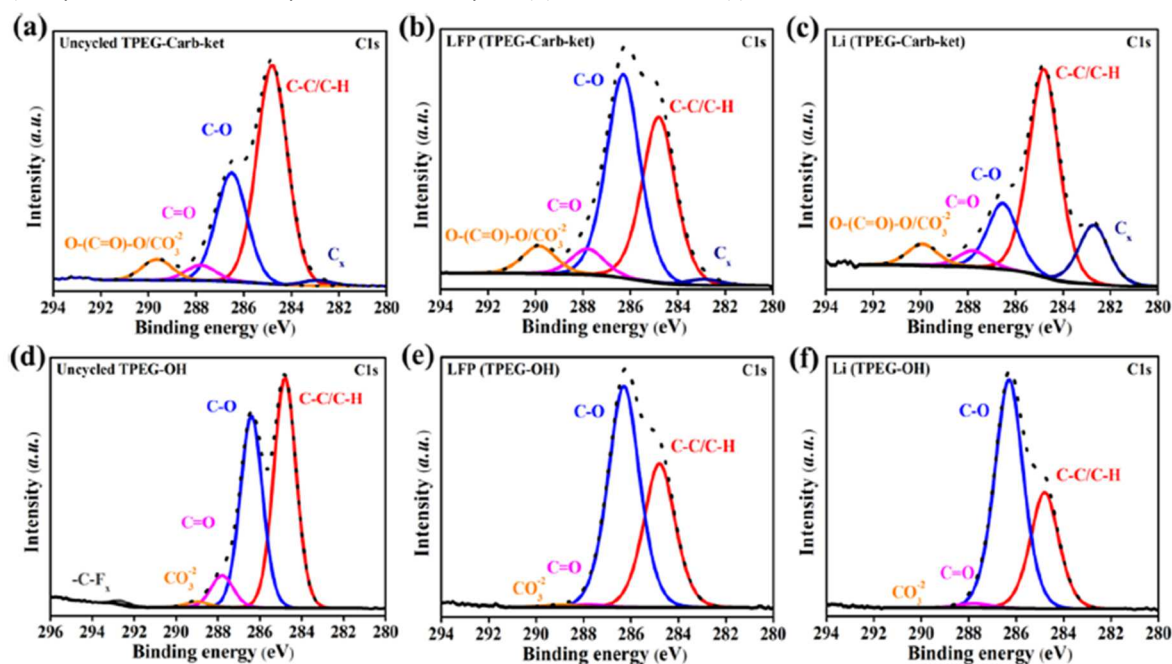
In order to gain more insight into those decomposition reactions at the interface between electrodes and solid electrolytes, AIMD simulations were performed on pure LFP cathode and Li metal anode surfaces (Figures S10 and S11). Those simulations confirmed a very strong attraction between the terminal groups of the TPEG-Carb-ket_{20%} and TPEG-OH_{20%} polymers and the electrode surface. On LFP, the oxygen and hydrogen atoms in the –OH terminal group of TPEG-OH_{20%} were found to coordinate significantly with the LFP surface with lithium and oxygen atoms, respectively. This could lead to a deprotonation reaction over time, which releases protons into the LFP electrode and can cause capacity fading. On Li metal, the decomposition of the –Carb–ket ending into carbonate was observed within 5 ps, indicating that this reaction is highly spontaneous and that further decomposition into inorganic carbonate is highly likely (Figure 9a). The following hypothesis was investigated by performing XPS on the surface of the LFP cathode and Li anode after cycling for more than 100+ cycles for both TPEG-carb-ket- and TPEG-OH-based cells, respectively, in comparison to the uncycled electrolyte surface at RT.

Figure 9. (a) Scheme depicting the decomposition of carbonate upon interaction with lithium. (b) Bar chart showing the carbon functional species on LFP and the Li electrode surface recorded from cycled disassembled cells with TPEG-Carb-ket and TPEG-OH.



The bar chart depicted in Figure 9b confirms the significant formation of carbonate/ester species in the case of TPEG-Carb-ket, which is also recorded in Li-LFP cycled cells, as highlighted in HR-XPS (Figure 10). Bader charge population analysis (Figure S12) indicated a more negative charge for oxygen atoms in the terminal groups on lithium, in particular for the –Carb–ket ending, which further confirms the higher reactivity toward the Li metal surface compared to the –OH ending. The same hypothesis was confirmed as we observed the formation of inorganic carbonate and additional carbide (C_x around 282.7 eV) at the surface of the uncycled electrolyte and cycled electrode with TPEG-Carb-Ket in comparison to TPEG-OH. This analysis presents a qualitative identification of all carbonate species with complexity in precise binding energy due to an overlapped spectrum. We speculate that those XPS investigations also support the cleavage of the carbonate into –O-(C=O)/C=O as a result of the reaction of Li along with the presence of stabilizing LIF species in the SEI at the Li metal surface (Figures 8 and 10). (64)

Figure 10. HR-XPS of carbon (a) uncycled TPEG-Carb-ket electrolyte; TPEG-Carb-ket led cycled (b) LFP cathode and (c) Li anode; (d) uncycled TPEG-OH electrolyte; TPEG-OH led cycled (e) LFP cathode and (f) Li anode.



Conclusions

In this study, we have highlighted the fundamental effect of the chain end functionality of a PEG-based PE for LMBs. We demonstrated in a combined experimental–computational approach that a carbonate-ketone terminal group acts in a sacrificial way by focusing the chain reactivity on itself and reacting more easily with the electrode surfaces due to its higher reactivity. This in turn leads to a stable SEI and allows for an efficient conductivity of lithium ions. The modified TPEG-Carb-ket not only offers a widened ESW (>4.48 V) but also provides better stable interfacial properties with lithium metal and LFP electrodes. The stripping and plating experiments, in addition to the aging study, by PEIS uncovered the crucial effect of the chain end modification for the stable SEI. The carbonate-ketone end-chain electrolyte offered a far more superior specific discharge capacity of ~ 118 mAh g $^{-1}$ with excellent Coulombic efficiency and a capacity retention of $>90\%$ for more than 100 cycles. These outstanding performances were supported by DFT calculations and AIMD simulations and further confirmed by postmortem studies of the electrolyte and electrodes by XPS. Organic carbonates have always been of interest due to their excellent coordination for electrolytes, and this report has contributed to elucidating their potential in tuning interfacial compatibility via facile end-chain chemistry. This work provides an interesting proof-of-concept and opens up direction toward the engineering of stable interfaces of PEs with organic carbonates for higher energy density and longer cycling LMBs.


Supporting Information

The Supporting Information is available free of charge at <https://pubs.acs.org/doi/10.1021/acsami.4c07927>.

- ¹NMR spectra, thermogravimetric analysis, Nyquist plots, temperature-dependent ionic conductivity, chronoamperometry and impedance measurements for transference number determination, stripping and plating experiments, galvanostatic charge–discharge voltage profiles, HR-XPS analysis, energy-minimized structures used in the quantum chemical calculations, AIMD simulation input structures, and Bader charge population analysis ([PDF](#))

Author Information

Corresponding Author

Jean-François Gohy - Institute of Condensed Matter and Nanoscience (IMCN), UCLouvain, Place L. Pasteur 1, 1348 Louvain-la-Neuve, Belgium;  <https://orcid.org/0000-0003-4169-1883>; Email: jean-francois.gohy@uclouvain.be

Notes

The authors declare no competing financial interest.

Acknowledgments

AR and JFG are grateful to INNOVIRIS (BRIDGE project) and to Service Public de Wallonie (Win4Excellence BATFACTORY 310153 project) for supporting this research. C.D. is the F.R.S.-FNRS Research Director. The authors of Liege thank F.N.R.S. for funding.

References

- (1) Armand, M.; Tarascon, J. M. Building better batteries. *Nature* 2008, 451 (7179), 652–657.
- (2) Choi, J. W.; Aurbach, D. Promise and reality of post-lithium-ion batteries with high energy densities. *Nat. Rev. Mater.* 2016, 1 (4), 16013.
- (3) Manthiram, A.; Yu, X.; Wang, S. Lithium battery chemistries enabled by solid-state electrolytes. *Nat. Rev. Mater.* 2017, 2 (4), 16103.
- (4) Harry, K. J.; Hallinan, D. T.; Parkinson, D. Y.; MacDowell, A. A.; Balsara, N. P. Detection of subsurface structures underneath dendrites formed on cycled lithium metal electrodes. *Nat. Mater.* 2014, 13 (1), 69–73.
- (5) Wacker, C. Achievements and Results Annual Report. Fraunhofer ISIT: Itzehoe, Germany, 2004.

- (6) Yamada, Y.; Wang, J.; Ko, S.; Watanabe, E.; Yamada, A. Advances and issues in developing salt-concentrated battery electrolytes. *Nature Energy* 2019, 4 (4), 269–280.
- (7) Choudhury, S.; Stalin, S.; Vu, D.; Warren, A.; Deng, Y.; Biswal, P.; Archer, L. A. Solid-state polymer electrolytes for high-performance lithium metal batteries. *Nat. Commun.* 2019, 10 (1), 4398.
- (8) Armand, M. Polymer solid electrolytes - an overview. *Solid State Ionics* 1983, 9–10, 745–754.
- (9) Arya, A.; Sharma, A. L. Polymer electrolytes for lithium ion batteries: a critical study. *Ionics* 2017, 23 (3), 497–540.
- (10) Liu, T.; Zhang, M.; Wang, Y. L.; Wang, Q. Y.; Lv, C.; Liu, K. X.; Suresh, S.; Yin, Y. H.; Hu, Y. Y.; Li, Y. S.; Liu, X. B.; Zhong, S. W.; Xia, B. Y.; Wu, Z. P. Engineering the Surface/Interface of Horizontally Oriented Carbon Nanotube Macrofilm for Foldable Lithium-Ion Battery Withstanding Variable Weather. *Adv. Energy Mater.* 2018, 8 (30), No. 1802349.
- (11) Bouchet, R.; Maria, S.; Meziane, R.; Aboulaich, A.; Lienafa, L.; Bonnet, J.-P.; Phan, T. N. T.; Bertin, D.; Gignes, D.; Devaux, D.; Denoyel, R.; Armand, M. Single-ion BAB triblock copolymers as highly efficient electrolytes for lithium-metal batteries. *Nat. Mater.* 2013, 12 (5), 452–457.
- (12) Li, W.; Wu, Y.; Wang, J.; Huang, D.; Chen, L.; Yang, G. Hybrid gel polymer electrolyte fabricated by electrospinning technology for polymer lithium-ion battery. *Eur. Polym. J.* 2015, 67, 365–372.
- (13) Marcinek, M.; Syzdek, J.; Marczewski, M.; Piszcz, M.; Niedzicki, L.; Kalita, M.; Plewa-Marczewska, A.; Bitner, A.; Wieczorek, P.; Trzeciak, T.; Kasprzyk, M.; Łęzak, P.; Zukowska, Z.; Zalewska, A.; Wieczorek, W. Electrolytes for Li-ion transport – Review. *Solid State Ionics* 2015, 276, 107–126.
- (14) Lu, D.; Shao, Y.; Lozano, T.; Bennett, W. D.; Graff, G. L.; Polzin, B.; Zhang, J.; Engelhard, M. H.; Saenz, N. T.; Henderson, W. A.; Bhattacharya, P.; Liu, J.; Xiao, J. Failure Mechanism for FastCharged Lithium Metal Batteries with Liquid Electrolytes. *Adv. Energy Mater.* 2015, 5 (3), No. 1400993.
- (15) Bai, P.; Li, J.; Brushett, F. R.; Bazant, M. Z. Transition of lithium growth mechanisms in liquid electrolytes. *Energy Environ. Sci.* 2016, 9 (10), 3221–3229.
- (16) Meyer, W. H. Polymer Electrolytes for Lithium-Ion Batteries. *Adv. Mater.* 1998, 10 (6), 439–448.
- (17) Murbach, M. D.; Schwartz, D. T. Analysis of Li-Ion Battery Electrochemical Impedance Spectroscopy Data: An Easy-to-Implement Approach for Physics-Based Parameter Estimation Using an Open-Source Tool. *J. Electrochem. Soc.* 2018, 165 (2), A297–A304.
- (18) Du, M.; Liao, K.; Lu, Q.; Shao, Z. Recent advances in the interface engineering of solid-state Li-ion batteries with artificial buffer layers: challenges, materials, construction, and characterization. *Energy Environ. Sci.* 2019, 12 (6), 1780–1804.
- (19) Dai, J.; Yang, C.; Wang, C.; Pastel, G.; Hu, L. Interface Engineering for Garnet-Based Solid-State Lithium-Metal Batteries: Materials, Structures, and Characterization. *Adv. Mater.* 2018, 30 (48), No. 1802068.

- (20) Li, Y.; Zhang, D.; Xu, X.; Wang, Z.; Liu, Z.; Shen, J.; Liu, J.; Zhu, M. Interface engineering for composite cathodes in sulfide-based all-solid-state lithium batteries. *Journal of Energy Chemistry* 2021, 60, 32–60.
- (21) Nakayama, M.; Wada, S.; Kuroki, S.; Nogami, M. Factors affecting cyclic durability of all-solid-state lithium polymer batteries using poly(ethylene oxide)-based solid polymer electrolytes. *Energy Environ. Sci.* 2010, 3 (12), 1995–2002.
- (22) Zhu, J.; He, S.; Tian, H.; Hu, Y.; Xin, C.; Xie, X.; Zhang, L.; Gao, J.; Hao, S.-M.; Zhou, W.; Zhang, L. The Influences of DMF Content in Composite Polymer Electrolytes on Li⁺-Conductivity and Interfacial Stability with Li-Metal. *Adv. Funct. Mater.* 2023, 33 (25), No. 2301165.
- (23) Zhao, X.; Wang, C.; Liu, H.; Liang, Y.; Fan, L.-Z. A Review of Polymer-based Solid-State Electrolytes for Lithium-Metal Batteries: Structure, Kinetic, Interface Stability, and Application. *Batteries Supercaps* 2023, 6 (4), No. e202200502.
- (24) Qin, S.; Yu, Y.; Zhang, J.; Ren, Y.; Sun, C.; Zhang, S.; Zhang, L.; Hu, W.; Yang, H.; Yang, D. Separator-Free In Situ Dual-Curing Solid Polymer Electrolytes with Enhanced Interfacial Contact for Achieving Ultrastable Lithium-Metal Batteries. *Adv. Energy Mater.* 2023, 13 (34), No. 2301470.
- (25) Zhou, W.; Wang, Z.; Pu, Y.; Li, Y.; Xin, S.; Li, X.; Chen, J.; Goodenough, J. B. Double-Layer Polymer Electrolyte for High-Voltage All-Solid-State Rechargeable Batteries. *Adv. Mater.* 2019, 31 (4), No. 1805574.
- (26) Henschel, J.; Peschel, C.; Klein, S.; Horsthemke, F.; Winter, M.; Nowak, S. Clarification of Decomposition Pathways in a State-of-the Art Lithium Ion Battery Electrolyte through ¹³C-Labeling of Electrolyte Components. *Angew. Chem., Int. Ed.* 2020, 59 (15), 6128–6137.
- (27) Yang, X.; Jiang, M.; Gao, X.; Bao, D.; Sun, Q.; Holmes, N.; Duan, H.; Mukherjee, S.; Adair, K.; Zhao, C.; Liang, J.; Li, W.; Li, J.; Liu, Y.; Huang, H.; Zhang, L.; Lu, S.; Lu, Q.; Li, R.; Singh, C. V.; Sun, X. Determining the limiting factor of the electrochemical stability window for PEO-based solid polymer electrolytes: main chain or terminal – OH group? *Energy Environ. Sci.* 2020, 13 (5), 1318–1325.
- (28) Fang, Z.; Luo, Y.; Liu, H.; Hong, Z.; Wu, H.; Zhao, F.; Liu, P.; Li, Q.; Fan, S.; Duan, W.; Wang, J. Boosting the Oxidative Potential of Polyethylene Glycol-Based Polymer Electrolyte to 4.36 V by Spatially Restricting Hydroxyl Groups for High-Voltage Flexible Lithium-Ion Battery Applications. *Adv. Sci.* 2021, 8 (16), No. 2100736.
- (29) Pozyczka, K.; Marzantowicz, M.; Dygas, J. R.; Krok, F. Ionic conductivity and lithium transference number of poly(ethylene oxide):LiTFSI system. *Electrochim. Acta* 2017, 227, 127–135.
- (30) Morioka, T.; Nakano, K.; Tominaga, Y. Ion-Conductive Properties of a Polymer Electrolyte Based on Ethylene Carbonate/ Ethylene Oxide Random Copolymer. *Macromol. Rapid Commun.* 2017, 38 (8), 1600652.
- (31) Boujioui, F.; Zhuge, F.; Damerow, H.; Wehbi, M.; Améduri, B.; Gohy, J.-F. Solid polymer electrolytes from a fluorinated copolymer bearing cyclic carbonate pendant groups. *Journal of Materials Chemistry A* 2018, 6 (18), 8514–8522.

- (32) Boujioui, F.; Damerow, H.; Zhuge, F.; Gohy, J.-F. Solid Polymer Electrolytes Based on Copolymers of Cyclic Carbonate Acrylate and n-Butylacrylate. *Macromol. Chem. Phys.* 2020, 221 (6), No. 1900556.
- (33) Ouhib, F.; Meabe, L.; Mahmoud, A.; Grignard, B.; Thomassin, J.-M.; Boschini, F.; Zhu, H.; Forsyth, M.; Mecerreyes, D.; Detrembleur, C. Influence of the Cyclic versus Linear Carbonate Segments in the Properties and Performance of CO₂-Sourced Polymer Electrolytes for Lithium Batteries. *ACS Applied Polymer Materials* 2020, 2 (2), 922–931.
- (34) Raj, A.; Panchireddy, S.; Grignard, B.; Detrembleur, C.; Gohy, J.-F. Bio-Based Solid Electrolytes Bearing Cyclic Carbonates for SolidState Lithium Metal Batteries. *ChemSusChem* 2022, 15 (18), No. e202200913.
- (35) Ngassam Tounzoua, C.; Grignard, B.; Brege, A.; Jerome, C.; Tassaing, T.; Mereau, R.; Detrembleur, C. A Catalytic Domino Approach toward Oxo-Alkyl Carbonates and Polycarbonates from CO₂, Propargylic Alcohols, and (Mono- and Di-)Alcohols. *ACS Sustainable Chem. Eng.* 2020, 8 (26), 9698–9710.
- (36) Frisch, G. W. T. M. J.; Schlegel, H. B.; Scuseria, G. E.; Robb, M. A.; Cheeseman, J. R.; Scalmani, G.; Barone, V.; Petersson, G. A.; Nakatsuji, H.; Li, X.; Caricato, M.; Marenich, A.; Bloino, J.; Janesko, B. G.; Gomperts, R.; Mennucci, B.; Hratchian, H. P.; Ortiz, J. V.; Izmaylov, A. F.; Sonnenberg, J. L.; Williams-Young, D.; Ding, F.; Lipparini, F.; Egidi, F.; Goings, J.; Peng, B.; Petrone, A.; Henderson, T.; Ranasinghe, D.; Zakrzewski, V. G.; Gao, J.; Rega, N.; Zheng, G.; Liang, W.; Hada, M.; Ehara, M.; Toyota, K.; Fukuda, R.; Hasegawa, J.; Ishida, M.; Nakajima, T.; Honda, Y.; Kitao, O.; Nakai, H.; Vreven, T.; Throssell, K.; Montgomery, J. A., Jr.; Peralta, J. E.; Ogliaro, F.; Bearpark, M.; Heyd, J. J.; Brothers, E.; Kudin, K. N.; Staroverov, V. N.; Keith, T.; Kobayashi, R.; Normand, J.; Raghavachari, K.; Rendell, A.; Burant, J. C.; Iyengar, S. S.; Tomasi, J.; Cossi, M.; Millam, J. M.; Klene, M.; Adamo, C.; Cammi, R.; Ochterski, J. W.; Martin, R. L.; Morokuma, K.; Farkas, O.; Foresman, J. B.; Fox, D. J.; Gaussian 16 Revision A.03, 2016.
- (37) Becke, A. D. Density-functional thermochemistry. III. The role of exact exchange. *J. Chem. Phys.* 1993, 98 (7), 5648–5652.
- (38) Parr, R. G.; Weitao, Y. *Density-Functional Theory of Atoms and Molecules*. Oxford University Press: 1995.
- (39) Kresse, G.; Furthmüller, J. Efficient iterative schemes for ab initio total-energy calculations using a plane-wave basis set. *Phys. Rev. B* 1996, 54 (16), 11169–11186.
- (40) Blöchl, P. E. Projector augmented-wave method. *Phys. Rev. B* 1994, 50 (24), 17953–17979.
- (41) Perdew, J. P.; Burke, K.; Ernzerhof, M. Generalized Gradient Approximation Made Simple [*Phys. Rev. Lett.* 77, 3865 (1996)]. *Phys. Rev. Lett.* 1997, 78 (7), 1396–1396.
- (42) Grimme, S.; Ehrlich, S.; Goerigk, L. Effect of the damping function in dispersion corrected density functional theory. *Journal of computational chemistry* 2011, 32 (7), 1456–1465.
- (43) Momma, K.; Izumi, F. VESTA 3 for three-dimensional visualization of crystal, volumetric and morphology data. *J. Appl. Crystallogr.* 2011, 44 (6), 1272–1276.

- (44) Tang, W.; Sanville, E.; Henkelman, G. A grid-based Bader analysis algorithm without lattice bias. *J. Phys.: Condens. Matter* 2009, 21 (8), No. 084204.
- (45) Ngassam Tounzoua, C.; Grignard, B.; Detrembleur, C. Exovynylene Cyclic Carbonates: Multifaceted CO₂-Based Building Blocks for Modern Chemistry and Polymer Science. *Angew. Chem., Int. Ed.* 2022, 61 (22), No. e202116066.
- (46) Gennen, S.; Grignard, B.; Tassaing, T.; Jérôme, C.; Detrembleur, C. CO₂-Sourced α -Alkylidene Cyclic Carbonates: A Step Forward in the Quest for Functional Regioregular Poly(urethane)s and Poly(carbonate)s. *Angew. Chem., Int. Ed.* 2017, 56 (35), 10394–10398.
- (47) Wong, D. H. C.; Vitale, A.; Devaux, D.; Taylor, A.; Pandya, A. A.; Hallinan, D. T.; Thelen, J. L.; Mecham, S. J.; Lux, S. F.; Lapides, A. M.; Resnick, P. R.; Meyer, T. J.; Kostecki, R. M.; Balsara, N. P.; DeSimone, J. M. Phase Behavior and Electrochemical Characterization of Blends of Perfluoropolyether, Poly(ethylene glycol), and a Lithium Salt. *Chem. Mater.* 2015, 27 (2), 597–603.
- (48) Boschin, A.; Johansson, P. Characterization of NaX (X: TFSI, FSI) – PEO based solid polymer electrolytes for sodium batteries. *Electrochim. Acta* 2015, 175, 124–133.
- (49) Rey, I.; Lassegues, J. C.; Grondin, J.; Servant, L. Infrared and Raman study of the PEO-LiTFSI polymer electrolyte. *Electrochim. Acta* 1998, 43 (10), 1505–1510.
- (50) Ruther, R. E.; Yang, G.; Delnick, F. M.; Tang, Z.; Lehmann, M. L.; Saito, T.; Meng, Y.; Zawodzinski, T. A.; Nanda, J. Mechanically Robust, Sodium-Ion Conducting Membranes for Nonaqueous Redox Flow Batteries. *ACS Energy Letters* 2018, 3 (7), 1640–1647.
- (51) Stolwijk, N. A.; Heddier, C.; Reschke, M.; Wiencierz, M.; Bokeloh, J.; Wilde, G. Salt-Concentration Dependence of the Glass Transition Temperature in PEO–NaI and PEO–LiTFSI Polymer Electrolytes. *Macromolecules* 2013, 46 (21), 8580–8588.
- (52) Mac Callum, J. R.; Vincent, C. A. Eds, In *Polymer Electrolyte Reviews 1*, Elsevier: Elsevier, 1987.
- (53) Karan, N. K.; Pradhan, D. K.; Thomas, R.; Natesan, B.; Katiyar, R. S. Solid polymer electrolytes based on polyethylene oxide and lithium trifluoro- methane sulfonate (PEO–LiCF₃SO₃): Ionic conductivity and dielectric relaxation. *Solid State Ionics* 2008, 179 (19), 689–696.
- (54) Miyamoto, T.; Shibayama, K. Free-volume model for ionic conductivity in polymers. *J. Appl. Phys.* 1973, 44 (12), 5372–5376.
- (55) Xi, J.; Qiu, X.; Cui, M.; Tang, X.; Zhu, W.; Chen, L. Enhanced electrochemical properties of PEO-based composite polymer electrolyte with shape-selective molecular sieves. *J. Power Sources* 2006, 156 (2), 581–588.
- (56) Zhao, Y.; Huang, Z.; Chen, S.; Chen, B.; Yang, J.; Zhang, Q.; Ding, F.; Chen, Y.; Xu, X. A promising PEO/LAGP hybrid electrolyte prepared by a simple method for all-solid-state lithium batteries. *Solid State Ionics* 2016, 295, 65–71.
- (57) Liu, H.; Cheng, X.-B.; Xu, R.; Zhang, X.-Q.; Yan, C.; Huang, J.Q.; Zhang, Q. Plating/Stripping Behavior of Actual Lithium Metal Anode. *Adv. Energy Mater.* 2019, 9 (44), No. 1902254.

- (58) Bieker, G.; Winter, M.; Bieker, P. Electrochemical in situ investigations of SEI and dendrite formation on the lithium metal anode. *Phys. Chem. Chem. Phys.* 2015, 17 (14), 8670–8679.
- (59) Leroy, S.; Martinez, H.; Dedryvere, R.; Lemordant, D.; Gonbeau, D. Influence of the lithium salt nature over the surface film formation on a graphite electrode in Li-ion batteries: An XPS study. *Appl. Surf. Sci.* 2007, 253 (11), 4895–4905.
- (60) Eshkenazi, V.; Peled, E.; Burstein, L.; Golodnitsky, D. XPS analysis of the SEI formed on carbonaceous materials. *Solid State Ionics* 2004, 170 (1), 83–91.
- (61) Wood, K. N.; Teeter, G. XPS on Li-Battery-Related Compounds: Analysis of Inorganic SEI Phases and a Methodology for Charge Correction. *ACS Applied Energy Materials* 2018, 1 (9), 4493–4504.
- (62) Shi, P.; Zhang, L.; Xiang, H.; Liang, X.; Sun, Y.; Xu, W. Lithium Difluorophosphate as a Dendrite-Suppressing Additive for Lithium Metal Batteries. *ACS Appl. Mater. Interfaces* 2018, 10 (26), 22201–22209.
- (63) Grissa, R.; Fernandez, V.; Fairley, N.; Hamon, J.; Stephant, N.; Rolland, J.; Bouchet, R.; Lecuyer, M.; Deschamps, M.; Guyomard, D.; Moreau, P. XPS and SEM-EDX Study of Electrolyte Nature Effect on Li Electrode in Lithium Metal Batteries. *ACS Appl. Energy Mater.* 2018, 1 (10), 5694–5702.
- (64) Bekaert, L.; Raj, A.; Gohy, J.-F.; Hubin, A.; De Proft, F.; Mamme, M. H. Assessing the Long-Term Reactivity to Achieve Compatible Electrolyte–Electrode Interfaces for Solid-State Rechargeable Lithium Batteries Using First-Principles Calculations. *J. Phys. Chem. C* 2022, 126 (19), 8227–8237.